Nucleic Acids Research, 2025, **53**, gkaf119
https://doi.org/10.1093/nar/gkaf119
Nucleic Acid Enzymes

Structural insights into human PNPase in health and disease

Yi-Ching Li[1], Chun-Hsiung Wang[2], Malay Patra[1], Yi-Ping Chen[1], Wei-Zen Yang[1], Hanna S. Yuan[1,3,*]

[1]Institute of Molecular Biology, Academia Sinica, Taipei, 11529, ROC, Taiwan
[2]Institute of Biological Chemistry, Academia Sinica, Taipei, 11529, ROC, Taiwan
[3]Graduate Institute of Biochemistry and Molecular Biology, National Taiwan University, Taipei, 10048, ROC, Taiwan
[*]To whom correspondence should be addressed. Email: hanna@sinica.edu.tw

Abstract

Human polynucleotide phosphorylase (hPNPase) is a 3′-to-5′ exoribonuclease located in mitochondria, where it plays crucial roles in RNA degradation and RNA import. Mutations in hPNPase can impair these functions, leading to various mitochondrial dysfunctions and diseases. However, the mechanisms by which hPNPase switches between its roles as an RNA-degrading enzyme and an RNA carrier, as well as how disease-associated mutations may affect these distinct functions, remain unclear. In this study, we present cryo-electron microscopy structures of hPNPase, highlighting the flexibility of its S1 domains, which cap the ring-like RNA-degradation chamber and shift between two distinctive open and closed conformations. We further demonstrate by small-angle X-ray scattering and biochemical analyses that the disease-associated mutations P467S and G499R impair hPNPase's stem-loop RNA-binding and degradation activities by limiting the S1 domain's ability to transition from an open to closed state. Conversely, the D713Y mutation, located within the S1 domain, does not affect the RNA-binding affinity of hPNPase, but diminishes its interaction with Suv3 helicase for cooperative degradation of structured RNA. Collectively, these findings underscore the critical role of S1 domain mobility in capturing structured RNA for degradation and import, as well as its involvement in mitochondrial degradosome assembly. Our study thereby reveals the molecular mechanism of hPNPase in RNA binding and degradation, and the multiple molecular defects that could be induced by disease-linked mutations in hPNPase.

Graphical abstract

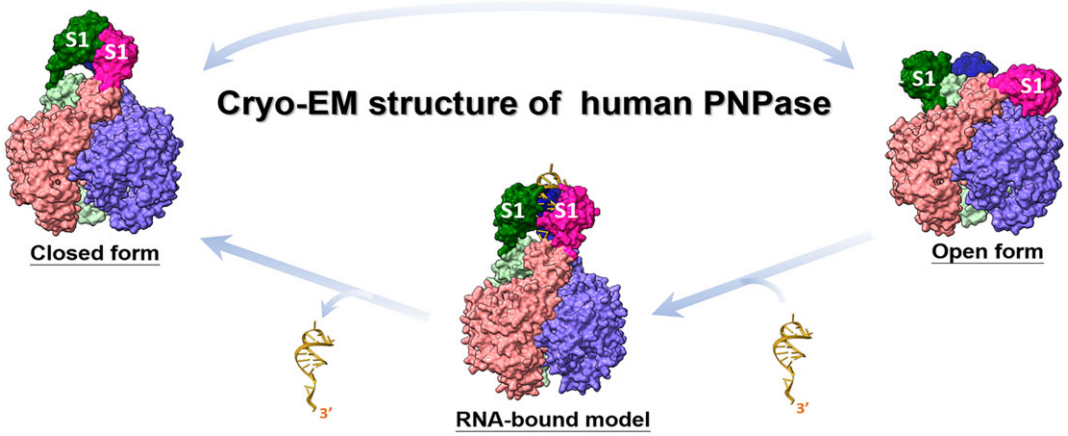

Introduction

Polynucleotide phosphorylase (PNPase) is a highly conserved 3′-to-5′ exoribonuclease, that plays a crucial role in RNA degradation. It catalyzes the processive removal of single ribonucleotides from the 3′ end of RNA via a phosphorolytic mechanism [1–3]. In both prokaryotes and eukaryotes, PNPase is primarily involved in RNA decay and RNA quality control [4, 5]. In bacteria, PNPase is an integral component of the RNA degradosome, responsible for bulk messenger RNA (mRNA) decay [6, 7], and it also participates in the processing and degradation of transfer RNA and ribosomal RNA (rRNA) [8, 9]. Interestingly, *Escherichia coli* PNPase also exhibits a paradoxical function in that it can switch from an RNA-degrading enzyme to an RNA carrier upon binding to

Received: November 25, 2024. **Revised:** January 23, 2025. **Editorial Decision:** February 4, 2025. **Accepted:** February 7, 2025

small regulatory RNAs (sRNAs) that are bound to the Hfq chaperon. Thus, *E. coli* PNPase can promote sRNA stability and regulate sRNA-mediated gene expression [10–12].

In mammals, PNPase contains an additional N-terminal mitochondrial localization signal (MLS) sequence that directs its localization to mitochondria [13]. The primary role of human PNPase (hPNPase) is to mediate RNA decay within the mitochondrial matrix, where it associates with Suv3 helicase to form a mitochondrial RNA (mtRNA) degradosome responsible for cooperative degradation of mtRNA exhibiting secondary structures [14–16]. hPNPase and Suv3 also restrict the levels of double-stranded mtRNA, preventing its escape into the cytoplasm where it could trigger antiviral signaling and an interferon response [17]. Moreover, akin to its bacterial counterparts, hPNPase plays an alternative role in the mitochondrial intermembrane space [18]. There, it facilitates translocation of non-coding RNAs into the mitochondrial matrix, including 5S rRNA, RNase P H1 RNA, and mitochondrial RNA processing (MRP) RNA, as well as microRNAs [19, 20]. These imported non-coding RNAs are crucial for processes such as mitochondrial DNA replication, RNA processing, and protein synthesis. Thus, hPNPase is vital for maintaining mitochondrial homeostasis [1].

It is intriguing how PNPase binds RNA and functions in different modes as an RNA-degrading enzyme or an RNA carrier. PNPase consists of five domains: two RNase PH-like domains (RNase PH1 and PH2); an α-helical (α) domain; a KH domain; and an S1 domain (see Fig. 1A). The crystal and cryogenic electron microscopy (cryo-EM) structures of PNPase from *Streptomyces antibioticus* [21], *E. coli* [22, 23], *Caulobacter crescentus* [24], *Mycobacterium smegmatis* [25], *Mycobacterium tuberculosis* [26], and *Homo sapiens* [27] reveal a characteristic trimeric ring-like architecture with a central constricted channel formed by the six RNase PH-like domains. The exoribonuclease active site is located within the RNase PH2 domain buried within the RNA-binding channel, with the Ser484 and R446 residues of hPNPase being critical for phosphate binding, and its Asp538 and Asp544 being responsible for Mg^{2+} binding [22, 27, 28]. The 3′ end of a single-stranded RNA (ssRNA) molecule is threaded through the central channel to reach the catalytic site located within one of the RNase PH2 domains of the trimeric assembly [22–24, 27]. Due to this narrow RNA-binding channel that can accommodate only ssRNA but not double-stranded RNA (dsRNA), hPNPase only degrades ssRNA and the 3′ overhangs (>10 nucleotides) of stem-loop RNA [27].

The S1 and KH domains of PNPase are involved in RNA binding, with the three KH domains together forming a stable KH pore that crowns the ring-like RNA-degrading chamber, which plays an important role in binding ssRNA and protein stability [27, 29]. Mutation of a single residue (G622D) in the conserved GXXG motif of the KH domain was found previously to impair the ssRNA-binding activity of hPNPase [27]. In contrast, the S1 domain has not been resolved in most crystal structures generated to date, indicating that it is highly dynamic [21–23, 25, 27]. Deletion of hPNPase's S1 domain does not affect ssRNA binding but it impairs binding of structured RNA, implying that the S1 domain is involved in interactions with RNA possessing secondary structures [29]. The cryo-EM structure of *E. coli* PNPase confirmed that the S1 domain is indeed flexible in the absence of RNA substrate [30]. However, upon binding to a Hfq-bound sRNA, the S1 and KH domains directly interact with the sRNA so that it is rerouted away from the active site to avoid degradation [30]. The distinct RNA-binding modes observed in *E. coli* PNPase, whereby ssRNA is bound within the narrow RNA-binding channel, whereas structured sRNA is bound by the KH and S1 domains outside of the RNA-degrading chamber, illustrate how bacterial PNPase can function either as an RNA-degrading enzyme or as an sRNA carrier.

Nevertheless, it is not clear how hPNPase switches its role between RNA degradation and RNA import. Due to the essential roles of hPNPase in mitochondria, it has been noted that biallelic missense and nonsense mutations in the *PNPT1* gene, which encodes hPNPase, are linked to a diversity of heterogeneous clinical symptoms, ranging from hearing loss to early-onset encephalopathy [31]. Two pathogenic homozygous mutations in hPNPase, Q387R and E475G, were first characterized in patients exhibiting hearing loss and respiratory-chain deficiency [32, 33]. Both Q387 and E475 are located within the RNase PH2 domain and at the trimeric interface, where they directly interact with residues of the neighboring protomers to stabilize trimer assembly (Q387 forms a hydrogen bond with R65, and E475 forms hydrogen bonds with K105 and N155). The Q387R and E475G mutations of hPNPase disrupt trimer formation, so that only defective dimers exhibiting impaired RNA-binding and degradation activities are assembled [29]. Heterozygous hPNPase variants have also been identified, including R136H/P140L that are associated with Leigh syndrome [34], Q254K/A510P that cause severe multisystem disease [35], G76D/R192* (where * indicates a nonsense mutation) that are related with delayed myelination and mitochondria dysfunctions [36] and D584G/M745T that are linked to multiple neurologic symptoms [37]. Residues R136 and P140 are located in the RNase PH1 domain, i.e. near catalytic residues R446, D538, and D544 within the active site. Thus, mutations of R136H and P140L reduce the catalytic activity of PNPase, leading to RNA processing defects and the classic respiratory chain deficiency associated with Leigh syndrome [34]. Several new disease-associated hPNPase variants have recently been identified, including P467H/S that are linked to Aicardi–Goutières syndrome (AGS) [38], as well as the heterozygous variants S70P/D713Y and G499R/A507S that elicit mitochondrial dsRNA accumulation along with upregulation of type I interferon response, resulting in multiple neurological disorders, including hypotonia and deafness [17]. Notably, some of these pathogenic hPNPase mutations, including P467H/S, G499R, and D713Y, are not located in the vicinity of the catalytic active site, RNA-binding channel, or trimeric interfaces. This raises intriguing questions about how these mutations lead to the mtRNA degradation or import defects that trigger various disease phenotypes.

In this study, we report the single-particle cryo-EM structures of full-length hPNPase, revealing its ring-like trimeric architecture capped by the flexible S1 domains, with these latter adopting one of two distinct open or closed conformations. Using small-angle X-ray scattering (SAXS) and biochemical assays, we further demonstrate that the disease-linked mutations P467S and G499R lead to defects in stem-loop RNA binding and degradation due to reduced S1 domain mobility. Additionally, we show that the D713Y mutation impairs the interaction between hPNPase and Suv3 helicase, thereby disrupting the cooperative degradation of structured RNA by these two enzymes. Our findings underscore the pivotal role of S1 domain mobility in capturing and binding struc-

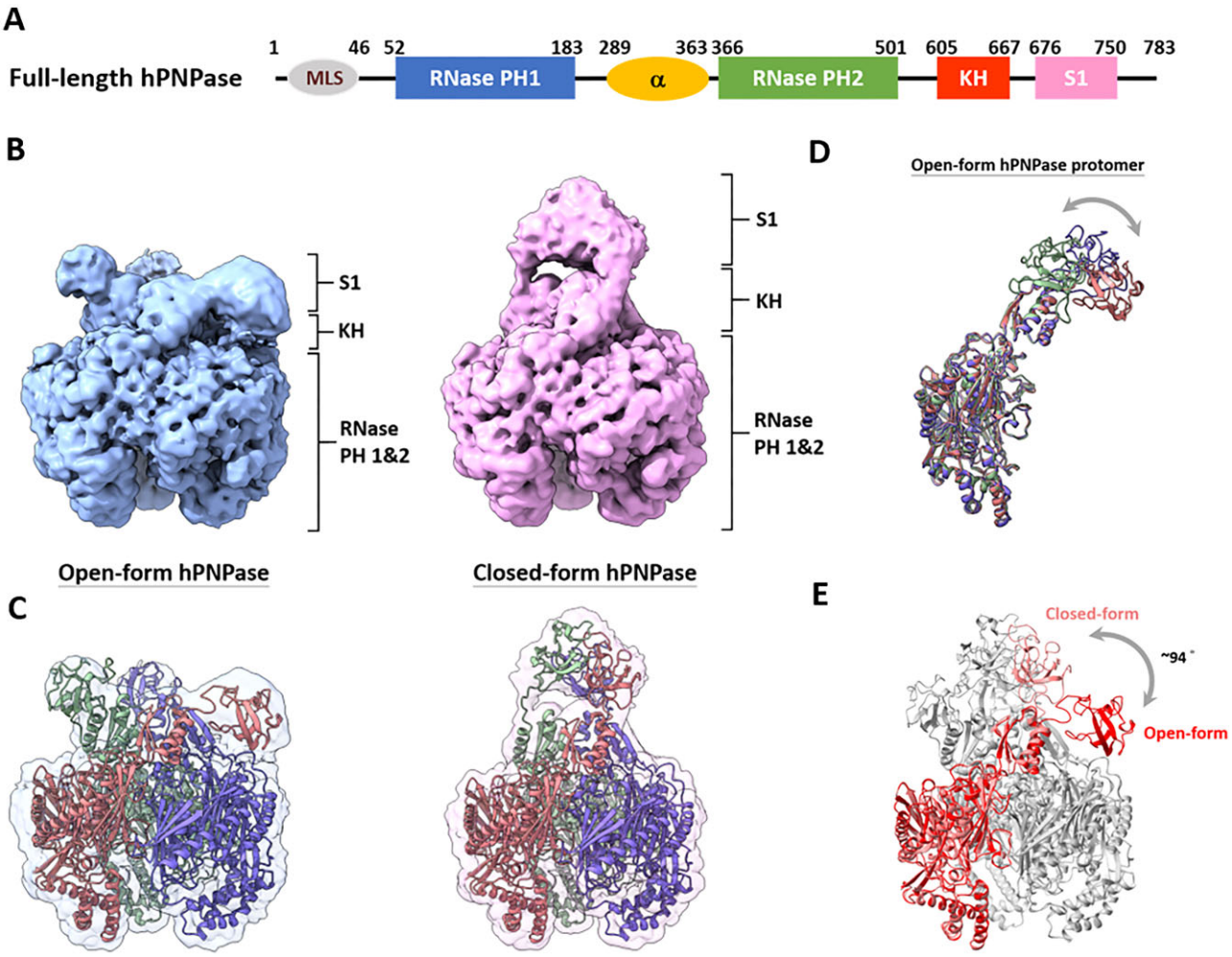

Figure 1. Cryo-EM structures of hPNPase. (**A**) The domain organization of hPNPase. (**B**) Cryo-EM density maps of hPNPase in two conformations, i.e. the open and closed forms, with estimated resolutions of 3.72–3.92 and 3.84 Å based on FSC 0.143 criterion, respectively. (**C**) Structural models of hPNPase in its two forms, overlaid with the cryo-EM maps. (**D**) Molecular motion of the S1 domain in one of the hPNPase protomers in the open conformation. (**E**) Aligned models of trimeric hPNPase in its open and closed forms, revealing significantly different conformations of the S1 domains, which rotate ~94° between the two states.

tured RNA, and they reveal a previously unknown function of the S1 domain in mediating cooperative RNA decay through interactions with Suv3. Collectively, our study provides structural insights into how hPNPase performs RNA binding and degradation, and how mutations may disrupt its functions and contribute to a diverse range of disease-related symptoms.

Materials and methods

Cloning, protein expression, and purification

The complementary DNA (cDNA) encoding full-length hPNPase (residues 46–783), but excluding its MLS, was amplified via polymerase chain reaction using Taq DNA polymerase (Stratagene). The amplified cDNA products were subcloned into the *NcoI* and *NotI* restriction sites of pET28b expression vector (Novagen), resulting in a plasmid encoding a C-terminal His-tagged hPNPase. Plasmids encoding the single hPNPase mutations P467S, G499R, and D713Y, as well as the double mutations P467S-S484A, G499R-S484A, and D713Y-S484A, were introduced into the wild-type hPNPase pET28b plasmid using the QuickChange site-directed mutagenesis kit (Stratagene). All constructs were transformed into *E. coli* strain BL21-CodonPlus (DE3)-RIPL (Stratagene). The transformed cells were then incubated overnight at 37°C in LB medium supplemented with 50 μg/ml kanamycin. The cell cultures were grown to an OD_{600} of 0.6 and then induced with 0.5 mM IPTG, followed by incubation at 18°C for 20 h for protein expression. Harvested cells were disrupted using a microfluidizer (Microfluidics M-110P) in a buffer containing 50 mM Tris (pH 7.4), 1 M NaCl, and 10 mM imidazole. The resulting cell lysate was centrifuged at 17 000 rpm for 30 min to remove cell debris, yielding a clarified supernatant for further purification steps.

All wild-type and mutant hPNPase protein variants were purified using similar chromatographic methods, as described below. Crude cell extracts were first loaded onto a His-Trap HP column (5 ml, GE Healthcare) for affinity purification, and hPNPase protein samples were eluted using a gradient of 0–500 mM imidazole in 50 mM Tris–HCl (pH 7.4) and 500 mM NaCl. The eluted fractions were then diluted 10-fold with a buffer containing 50 mM Tris–HCl (pH 7.4) and 10 mM ethylenediaminetetraacetic acid (EDTA). Next, the protein sample was passed through a HiTrap Heparin HP column (5 ml, GE Healthcare), and hPNPase was eluted using

a gradient of 0–1 M NaCl in 50 mM Tris–HCl (pH 7.4) and 10 mM EDTA. Protein fractions were collected and diluted 10-fold with 25 mM 4-(2-Hydroxyethyl)piperazine-1-ethanesulfonic acid (HEPES) (pH 7.0) and 1 M ammonium sulfate [$(NH_4)_2SO_4$], and then loaded onto the Phenyl HP column (5 ml, GE Healthcare). The hPNPase proteins were eluted using a gradient of 1–0 M $(NH_4)_2SO_4$ in 25 mM HEPES (pH 7.0). The purified hPNPase sample was concentrated to 0.5 ml and further purified via gel filtration on a Superdex 200 Increase 10/300 GL column (GE Healthcare), with a running buffer of 20 mM HEPES (pH 7.4) and 300 mM potassium chloride (KCl) (see Supplementary Fig. S1). The purified protein samples were concentrated to suitable concentrations and stored at −80°C until further use.

Cryo-electron microscopy sample preparation and data collection

Wild-type hPNPase samples were prepared at a concentration of 5 mg/ml in a buffer containing 20 mM HEPES (pH 7.4), 2.5 mM $MgCl_2$, 150 mM KCl, and 2 mM dithiothreitol (DTT). A 3-μl aliquot of the sample was applied to glow-discharged UltrAufoil® R 2/2, 200 Mesh, Au grids. Excess sample was removed by blotting with a FEI Vitrobot system (Thermo Fisher Scientific), with a 3-s blot time and a blot force of +2. This step was performed immediately after the addition of 8 mM CHAPSO (3-([3-cholamidopropyl]dimethylammonio)-2-hydroxy-1-propanesulfonate) to the protein sample. CHAPSO was added to prevent hPNPase from adhering to the air–water interface during grid preparation, ensuring optimal sample quality for subsequent structural analysis. The chamber conditions were set at 4°C with 100% humidity.

Cryo-EM grids were initially screened using a 200 keV Talos Arctica transmission electron microscope equipped with a Falcon III detector (Thermo Fisher Scientific) in linear mode. Images were recorded at a nominal magnification of 120 000×, yielding a pixel size of 0.86 Å/pixel, with a defocus setting of −2.5 μm. Suitable grids were then selected for high-resolution data collection using a 300 keV Titan Krios transmission electron microscope (Thermo Fisher Scientific) hosting a K3 detector (with GIF Bio-Quantum Energy Filters, Gatan) operating in super-resolution mode (gun lens 4, spot size 4, C2 aperture 50 μm) using EPU-2.7.0 software (Thermo Fisher Scientific). The raw movie stacks were recorded at a magnification of 105 000×, corresponding to a pixel size of 0.83 Å/pixel (super-resolution 0.415 Å/pixel). A defocus range of −1.6 to −2.2 μm was applied, and the slit width of the energy filter was set to 15 eV. Fifty frames of non-gain-normalized tiff stacks were recorded with a dose rate of ∼27.8 $e^-/Å^2$ per second and the total exposure time was set to 1.8 s, resulting in an accumulated dose of ∼50 $e^-/Å^2$ (∼1.0 $e^-/Å^2$ per frame). A detailed summary of the cryo-EM data acquisition parameters is provided in Supplementary Table S1.

Single-particle image processing, 3D reconstruction, atomic model building, and refinement

The super-resolution image stacks were corrected for motion and then dose-weighted using MotionCor2 [39], employing a 7 × 5 patch and two-fold binning, resulting in a final pixel size of 0.83 Å. The motion-corrected micrographs were subsequently imported into cryoSPARC [40] for single-particle reconstruction. The contrast transfer function (CTF) was estimated from the motion-corrected images using the "Patch CTF estimation" tool in cryoSPARC. Particles were extracted with a box size of 384 pixels for 2D classification. After multiple rounds of 2D classification, poor-quality 2D class averages were discarded, and the remaining particles were used for *ab initio* map generation, followed by 3D heterogeneous refinement (with separation into three distinct classes). Poor 3D classes were further removed through additional rounds of 3D heterogeneous refinement, and good particles were merged for further analysis. Another round of 2D classification was performed to remove any residual bad particles. Good particles were refined using 3D non-uniform refinement without imposed symmetry. Subsequently, the particles underwent C3 symmetry expansion, followed by focused or masked classification without alignments to enhance resolution of the S1 domain. Simultaneously, polished particles were subjected to symmetry expansion and 3D variability analysis using six modes and a 6 Å resolution limit. The resulting 3D density maps were visualized using ChimeraX [41]. A detailed workflow for single-particle image processing and cryo-EM reconstruction procedures is provided in Supplementary Fig. S2.

The coordinate model was constructed using the crystal structure of PNPase-ΔS1 (PDB ID: 3U1K) [27] as a template, combined with the S1 domain predicted by AlphaFold2 [42]. Rigid body docking of these components was performed using ChimeraX [41]. To further improve the global fit of the S1 domains, an automated molecular dynamics-based tool, Namdinator, was used [43]. The overall structure was refined using the Phenix software suite [44], with COOT [45] deployed for manual adjustments. The statistics for model validation, including real-space refinement metrics, were derived from the final output files generated by PHENIX [44]. Visualization of the structures, along with the creation of images and movies, was performed using ChimeraX [41] and PyMOL. All relevant statistics for cryo-EM reconstructions and model refinement are summarized in Supplementary Table S1.

Measurement of RNA-binding affinity of hPNPase by fluorescence polarization

The RNA-binding affinities of PNPase-S484A, PNPase-P467S-S484A, PNPase-G499R-S484A, and PNPase-D713Y-S484A for single-stranded and stem-loop RNAs were determined by measuring changes in fluorescence polarization (FP) using a Paradigm plate reader (Molecular Devices). The 30-nucleotide (nt) ssRNA substrate with a sequence of 5′-FAM-$(U)_{30}$–3′ was labeled with fluorescein at its 5′ end. The stem-loop RNA with a stem-loop motif of MRP RNA (sequence 5′-FAM-GAGCGUAUCCGCUC$(U)_{20}$–3′, in which underlined nucleotides represent base pairs in the stem region) was similarly labeled at the 5′ end. These RNAs (2 nM) were mixed individually with hPNPase in various concentrations in a buffer containing 20 mM Tris–HCl (pH 7.4), 50 mM KCl, 100 μg/ml bovine serum albumin (BSA), 0.1 mM EDTA, 1 mM DTT, 10% glycerol, and 2 mM $MgCl_2$. The hPNPase-RNA mixtures were incubated at 37°C for 30 min, and the FP signals were measured at 538 nm with the excitation wavelength at 485 nm. These experiments were performed in triplicate in a 384-well OptiPlate-Black (Perkin-Elmer) with a final reaction volume of 60 μl per well. Dissociation constant (K_d) values were determined by plotting FP against protein concentrations, and the binding curve was fitted by a one-site binding model with a Hill slope using the GraphPad Prism 9 software.

FP was calculated using equation (1):

$$\mathrm{mFP} = 1000 \times \left[\left(I_{\mathrm{para}} - I_{\mathrm{perp}} \right) / \left(I_{\mathrm{para}} + I_{\mathrm{perp}} \right) \right], \quad (1)$$

where I_{para} and I_{perp}represent the fluorescence intensities measured in the parallel and perpendicular planes, respectively. The resulting FP values were plotted against the hPNPase concentration, and the binding curves were fitted to derive K_{d}values using equation (2):

$$y = \mathrm{FP}_{\mathrm{min}} + \left[\left(\mathrm{FP}_{\mathrm{max}} - \mathrm{FP}_{\mathrm{min}} \right) / \left(1 + \left(x / K_{\mathrm{d}} \right)^{n} \right) \right], \quad (2)$$

where y is the FP value at a given protein concentration, $\mathrm{FP}_{\mathrm{max}}$ and $\mathrm{FP}_{\mathrm{min}}$are the maximum and minimum FP values, x is the concentration of hPNPase, $K_{\mathrm{d}}$is the dissociation constant, and n is the Hill coefficient.

For the competition binding assay, 2 nM fluorescein-labeled RNA was mixed with PNPase at a concentration of 0.625 μM for ssRNA and 2.5 μM for stem-loop RNA. These protein-RNA mixtures were then incubated with varying concentrations of unlabeled RNA. After 30 min of incubation, FP signals were measured. The FP values were plotted against the logarithm of unlabeled RNA concentrations using a nonlinear regression model. The Ki values were calculated from the binding-competitive model using GraphPad Prism 9 software.

RNase activity assays

For the RNA degradation assays, different concentrations of PNPase proteins (ranging from 0.2 to 0.8 μM), including hPNPase, PNPase-P467S, PNPase-G499R, and PNPase-D713Y, were incubated with either a 30-nt fluorescein-labeled ssRNA with the sequence of 5′-FAM-U_{30}-3′ (10 nM, purchased from Dharmacon) or a stem-loop RNA with the sequence of 5′-FAM-GAGCGUAUCCGCUC$(U)_{20}$–3′. The RNA degradation reactions were carried out for 30 min at 37°C in a reaction buffer containing 20 mM Tris–HCl (pH 7.5), 50 mM NaCl, 1 mM DTT, 2 mM NaH_2PO_4, and 0.25 mM $MgCl_2$. The RNA degradation reactions were stopped by adding 2× urea loading dye (Thermo Fisher Scientific) and heating the samples at 90°C for 3 min. The samples were then loaded onto a 15% TBE-urea polyacrylamide denaturing gel for electrophoresis. After separation, the gel was scanned using a Typhoon FLA 9000 system (GE Healthcare) to visualize the degradation products.

For RNA degradation by the Suv3-hPNPase complex, 0.1 μM hPNPase alone, or a mixture of wild-type hPNPase (or hPNPase mutants) and Suv3, was incubated with 50 nM of 5′-end fluorescein-labeled dsRNA. The reactions were performed at 37°C in a reaction buffer containing 20 mM Tris–HCl (pH 7.5), 50 mM NaCl, 1 mM DTT, 2 mM NaH_2PO_4, 0.25 mM $MgCl_2$, and 5 mM adenosine triphosphate (ATP). The reactions were terminated by adding an equal volume of 2× urea loading dye (Thermo Fisher Scientific) at different time points (0, 15, 30, and 45 min) and heating the samples at 90°C for 3 min. The samples were then loaded onto a 15% TBE-urea polyacrylamide denaturing gel for electrophoresis. RNA degradation patterns were visualized using a Typhoon FLA 9000 scanner (GE Healthcare). The RNA substrates used in the degradation assays were purchased from Dharmacon with sequences: 5′-FAM-GCGUCUGCACGUAUGCCACCACACCAGGAGAGGAGAGGAG-3′ and 5′-GGUGUGGUGGCAUACGUGCAGACGC-3′. These two RNA strands were annealed to generate a 25-basepair RNA duplex with a 15-nt 3′ overhang.

Small-angle X-ray scattering

SAXS data were recorded at the SAXS beamline TPS-23A, which was coupled to a high-performance liquid chromatography system that was connected to an Agilent-Bio SEC-3 300 Å column at the National Synchrotron Radiation Research Center in Hsinchu, Taiwan. All the samples, including hPNPase, hPNPase-P467S, hPNPase-G499R, and hPNPase-D713Y, were purified to high homogeneity and concentrated to 5 mg/ml in a buffer containing 20 mM HEPES (pH 7.4) and 300 mM KCl. To prevent freeze-thaw cycles, all protein samples were freshly purified prior to SAXS measurements. SAXS data were collected at a wavelength of ∼1 Å, with a total of 120 frames recorded at 2 s of exposure for each sample. Selected frames were merged and analyzed for initial radius of gyration (R_{g}) estimation using the PRIMUS program [46]. The maximum dimension (Dmax) and the $P(r)$ distance distribution were determined using the GNOM program [47]. Ensemble optimization method (EOM) analysis was performed using the web interface of EMBL Hamburg [48]. For that analysis, the crystal structure of PNPase-ΔS1 (PDB ID: 3U1K) [27] and the homology-modeled S1 domain (obtained via the SWISS-MODEL web server based on the crystal structure of the S1 domain in *Coxiella burnetii* PNPase, PDB ID: 4NBQ) [49] were utilized as rigid bodies in the ensemble search. A total of 10 000 models were generated, and the SAXS profiles of these models were fitted to the measured SAXS profiles to identify the best-fitting models. Two conformational subsets of hPNPase, designated as open and closed, were selected, and their ensemble provided fitting curves that closely matched the experimental SAXS data (see Fig. 4C).

CD spectroscopy

Far-UV circular dichroism (CD) spectra from 260 to 190 nm were recorded on an on JASCO J-1500 spectropolarimeter (Jasco International Co., Japan). All measurements were conducted in a 1-mm quartz cuvette at 20°C. The protein samples in 20 mM phosphate buffer (pH 7.4) were set to 5 μM for the hPNPase (wild type, S484A, P467S, G499R, or D713Y). Appropriate baseline correction with aqueous buffer solution was performed to rectify the CD spectra. All experiments were performed in triplicate. Secondary structure compositions were estimated and analyzed using DichroWeb [50]. Thermal denaturation was conducted by monitoring CD signals at 222 nm from 10 to 95°C. Tm values were calculated using the maximum of the first derivative of the CD signal.

Microscale thermophoresis assay

The affinity of the purified hPNPase proteins—including hPNPase, PNPase-P467S, PNPase-G499R, and PNPase-D713Y—for Suv3 was assessed using the Monolith NT.115pico system from Nanotemper Technologies. A total of 3.5 nM of Alexa647-labeled Suv3 was added to a 16-step serial dilution of wild-type or mutant hPNPase prepared through a 1:1 serial concentration gradient. The samples were incubated at room temperature for 30 min before being loaded into Monolith NT standard-treated capillaries. Measurements were performed at 25°C in a buffer consisting of 20 mM Tris (pH 8.0), 50 mM NaCl, 0.05% Tween 20, and 0.25% BSA, utilizing 20% light emitting diode (LED) power and medium microscale thermophoresis (MST) power settings. The assay was repeated independently three times, and the resulting dose-response curves were fitted to a one-site binding model to

extract dissociation constant (K_d) values. The analysis was conducted using MO.Affinity Analysis software (v2.3) and SigmaPlot 10.0 software.

Results

Cryo-EM structures of hPNPase reveal flexible S1 domains with open and closed conformations

Although crystal structures of hPNPase have been reported previously [27, 29], they only encompass the catalytic core and lack visible electron densities for the S1 domains. Given the crucial roles of both the KH and S1 domains in RNA substrate capture and autoregulation [51], we aimed to determine the structure of full-length hPNPase by single-particle cryo-EM. To do so, we expressed and purified a C-terminal His-tagged version of full-length hPNPase (residues 46–783), excluding the N-terminal mitochondrial localization sequence, which formed a stable homotrimer (Supplementary Fig. S1). Utilizing this homogeneous trimeric sample, we resolved cryo-EM structures of hPNPase, revealing the S1 domain in one of two distinct conformations, i.e. open or closed (Fig. 1, Supplementary Fig. S2 and Supplementary Table S1).

Using a conventional method to calculate a reconstruction map from cryo-EM images, we identified and classified three major conformations through 3D classification: an open form (from 911 400 particles), a closed form (811 762 particles), and a compact form without a visible protruding S1 domain (387 683 particles) (Supplementary Fig. S2B). We proceeded with iterative refinement of the open and closed forms without imposing symmetry to prevent misinterpretation. The densities corresponding to the S1 domains were blurred, implying flexible conformations. To better resolve these densities, we first conducted C3 symmetry reconstruction, then applied C3 symmetry expansion, and performed masked 3D classification using cryoSPARC v3.3.2 [40]. This approach allowed us to resolve the S1 domain into three distinct substates in the open-form structure of hPNPase (Supplementary Fig. S2C). The density for the S1 domain was enhanced for these substates, resulting in an improvement to 3.72–3.92 Å for the overall resolution, as estimated based on the gold-standard Fourier shell correlation (FSC) curve at a 0.143 criterion. The high-resolution maps in the core and KH domain at a resolution of 3.5 Å enabled unambiguous tracing of the polypeptide chain, with well-defined densities for bulky side chains (Supplementary Figs S3A and S4A). The improved cryo-EM maps also allowed for precise local rigid-body docking and molecular dynamics fitting of the S1 domains in the combined focused maps, with local resolutions ranging from 4.5 to 7.0 Å (Fig. 1B and C, and Supplementary Fig. S3A). Superimposing each protomer in the trimeric hPNPase structure revealed slight molecular motions of the S1 domains in the open-form structures, rotating ∼60° (Fig. 1D and Supplementary Fig. S5) and highlighting dynamic adjustments of the S1 domains above the hPNPase core in the open conformation.

We also performed C3 symmetry reconstruction, followed by C3 symmetry expansion and the use of masked 3D classification tools to analyze the closed-form structure of hPNPase, resulting in the identification of three substates (Supplementary Fig. S2D). The best substate was refined to an overall resolution of 3.84 Å, as estimated based on the FSC 0.143 criterion. The comparison between the closed and open forms of hPNPase structures revealed a similar overall architecture within the RNA-degradation chamber, which is formed by the RNase PH1, RNase PH2, α, and KH domains. This analysis resulted in a root-mean-square difference of 1.53 Å across 1 647 Cα atoms. However, the S1 domains exhibited substantial movement, characterized by an ∼94° rotation within a loop region (residues 626–631) between the KH and S1 domain (Fig. 1E). In the closed conformation, the three S1 domains interact closely with one another, whereas they are positioned further apart in the open conformation and closer to the RNase PH2 domains of adjacent protomers. This significant movement highlights the S1 domain's ability to undergo large conformational changes, transitioning between open and closed states.

Disease-linked P467S and G499R mutations in hPNPase impair the enzyme's stem-loop RNA-binding and degradation activities

The molecular mechanisms underlying the disease-linked mutations P467S, G499R, and D713Y remained poorly understood. Mapping these mutations onto our cryo-EM structure of hPNPase in its open conformation revealed that P467S and G499Y are located in loop regions on the surface of the RNase PH2 domain, whereas D713 is situated on the surface of the S1 domain (Fig. 2A). Notably, all three mutations are positioned far from the RNA-binding and cleavage sites of hPNPase. To assess if these disease-associated mutations affect the RNA-binding and degradation activities of hPNPase, we expressed and purified the single-point hPNPase mutants carrying the respective mutations: PNPase-P467S, PNPase-G499R, and PNPase-D713Y. Additionally, to measure the binding affinity between hPNPase and RNA, we generated double-point mutants incorporating an S484A mutation, which disrupts the enzyme's phosphate-binding and RNA-degradation activities, i.e. PNPase-P467S-S484A, PNPase-G499R-S484A, and PNPase-D713Y-S484A, respectively. All recombinant proteins were purified to high homogeneity using chromatographic methods, and they formed stable homotrimers, as confirmed by gel filtration profiles (Supplementary Fig. S1).

To determine if the mutations affect hPNPase's RNA-binding affinity, we measured binding between hPNPase and RNA by monitoring changes in FP signals using a fluorescein-labeled RNA upon protein-RNA interactions. Two RNA substrates were prepared: a 5′-end fluorescein-labeled 30-nt ssRNA [5′-FAM-$(U)_{30}$–3′]; and a stem-loop RNA containing the stem-loop motif of MRP RNA [5′-FAM-MRP-$(U)_{20}$–3′]. The inactive PNPase-S484A, along with the disease-associated mutants, PNPase-P467S-S484A, PNPase-G499R-S484A, and PNPase-D713Y-S484A, all demonstrated similar binding affinities to the ssRNA, with dissociation constant values (K_d) ranging from 0.069 to 0.089 μM, indicating that these mutations did not significantly alter the enzyme's binding affinity for ssRNA (Fig. 2C). Competition experiments using unlabeled ssRNA and stem-loop RNA were conducted, confirming that the changes in FP signals were indeed a result of the binding between hPNPase and RNA substrates (Supplementary Fig. S6). Moreover, PNPase-S484A and PNPase-D713Y-S484A showed comparable affinities for the stem-loop RNA ($K_d = 0.422 \pm 0.04$ and 0.581 ± 0.082 μM, respectively). In contrast, the PNPase-P467S-S484A ($K_d = 1.743 \pm 0.134$ μM) and PNPase-G499R-S484A ($K_d = 1.742 \pm 0.179$ μM) mutants exhibited an ∼4-fold

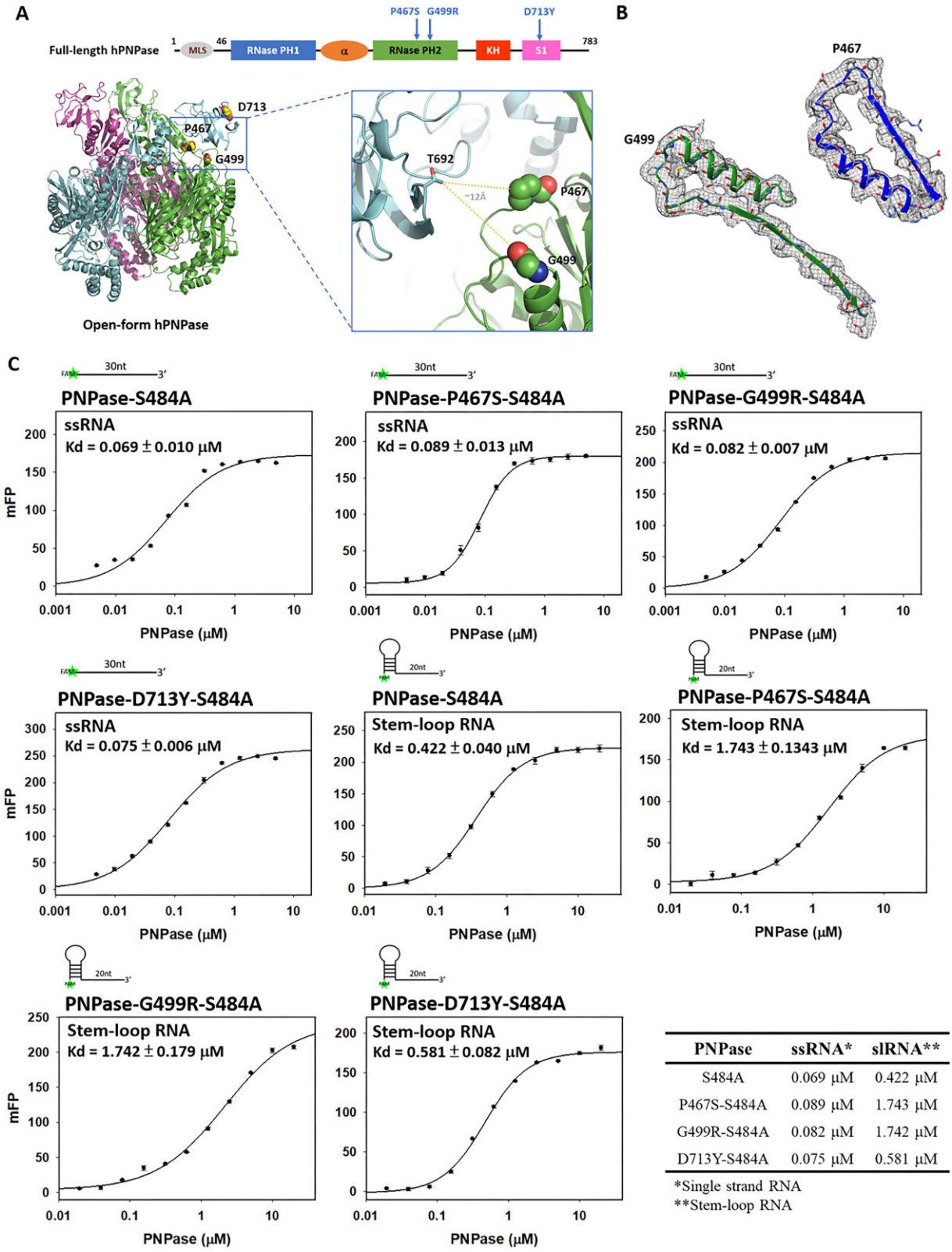

PNPase	ssRNA*	slRNA**
S484A	0.069 μM	0.422 μM
P467S-S484A	0.089 μM	1.743 μM
G499R-S484A	0.082 μM	1.742 μM
D713Y-S484A	0.075 μM	0.581 μM

*Single strand RNA
**Stem-loop RNA

Figure 2. RNA-binding affinities of the disease-linked hPNPase mutants. (**A**) The disease-linked mutations, i.e. P467S, G499R, and D713Y, are located in the RNase PH2 domain and the S1 domain. Mapping to the cryo-EM structure of hPNPase in the open conformation, residues P467 and G499 are located on the surface of the RNase PH2 domain and close to the S1 domain of the adjacent protomer, whereas D713 is positioned on the surface of the S1 domain. (**B**) Selected regions of the model and corresponding cryo-EM density reveal that the two disease-linked residues P467 and G499 are located in loop regions in the RNase PH2 domain. (**C**) The binding affinities between hPNPase and RNA were measured by monitoring changes in FP signals (in mFP units) upon mixing a fluorescein-labeled ssRNA (2 nM) or stem-loop RNA (2 nM) with hPNPase (0–5 μM for ssRNA and 0–20 μM for stem-loop RNA, two-fold dilution) using logarithmic scale. Two RNA substrates were used: a 5′-end fluorescein-labeled 30-nt ssRNA [5′-FAM-(**U**)$_{30}$–3′] or a stem-loop RNA containing the stem-loop motif of MRP RNA [5′-FAM-MRP-(**U**)$_{20}$–3′]. The error bar in each figure represents mean ± standard deviation (SD) from three independent experiments.

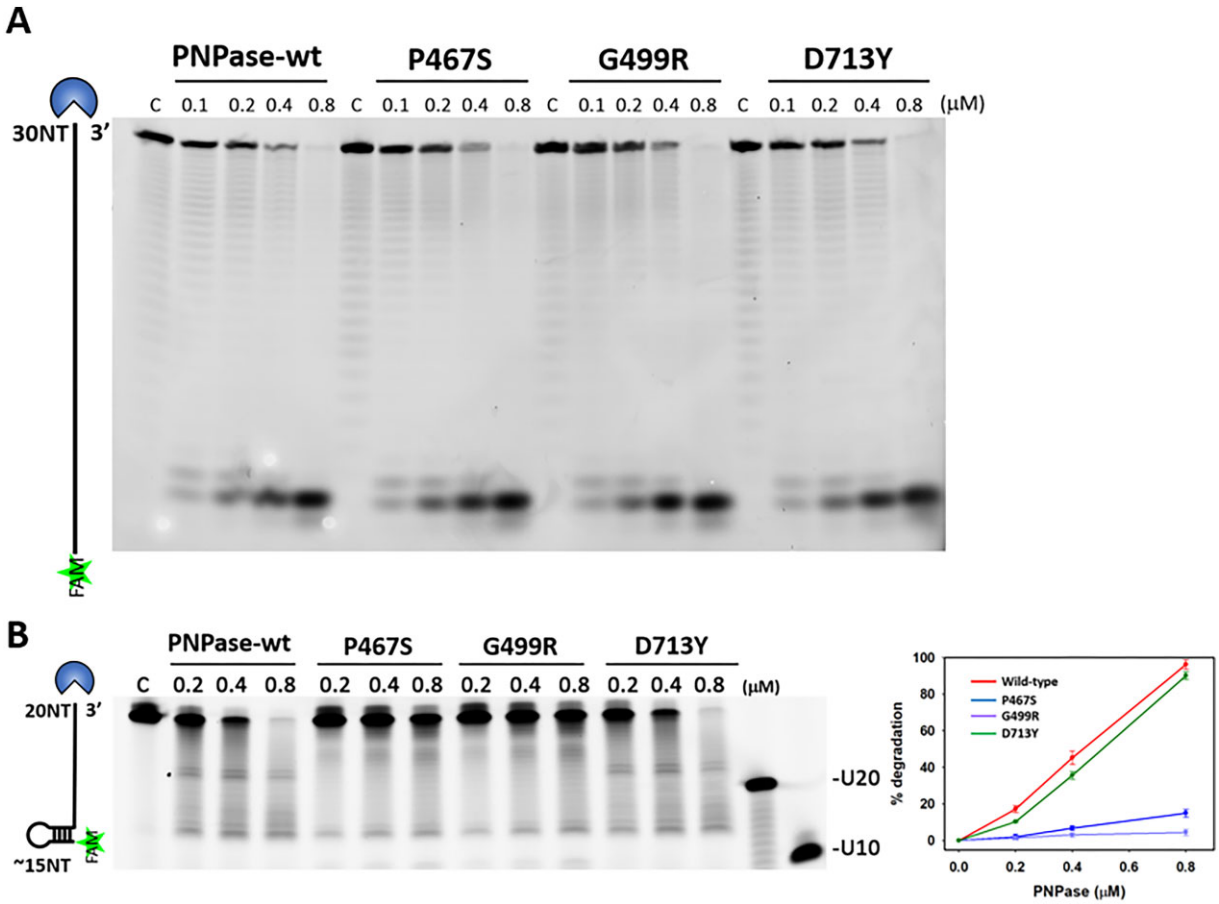

Figure 3. Disease-linked hPNPase mutants P467S and G499R exhibited impaired stem-loop RNA degradation activities. (**A**) Wild-type and mutated hPNPase (0.2–0.8 μM) degraded the ssRNA [5′-FAM-(**U**)$_{30}$–3′] to similar extends. (**B**) Wild-type hPNPase and D713Y mutant degraded stem-loop RNA [5′-FAM-MRP-(**U**)$_{20}$–3′] to similar extends. However, the hPNPase mutants, P467S and G499R, exhibited impaired stem-loop RNA degradation activities. The right panel displays a graph illustrating the degradation percentage of stem-loop RNA substrates by wild-type and mutated hPNPase. The error bars represent mean ± SD obtained from three independent experiments.

decrease in affinity for the stem-loop RNA compared to PNPase-S484A ($K_d = 0.42 \pm 0.040$ μM) (Fig. 2C). These results indicate that though the P467S and G499R mutations in hPNPase do not affect ssRNA binding, they significantly reduce the enzyme's binding affinity for stem-loop RNA.

To evaluate the impact of the mutations on RNA degradation, we incubated hPNPase with fluorescein-labeled ssRNA and stem-loop RNA in a degradation buffer at 37°C for 30 min. Wild-type hPNPase, as well as the three single-point mutants (PNPase-P467S, PNPase-G499R, and PNPase-D713Y), degraded the ssRNA substrate to a similar extent (Fig. 3A). In the stem-loop RNA degradation experiment, both wild-type hPNPase and the PNPase-D713Y mutant presented comparable degradation capacities. In contrast, the PNPase-P467S and PNPase-G499R mutants exhibited significantly reduced degradation activity, in a concentration-dependent manner, toward the stem-loop RNA compared to wild-type hPNPase (Fig. 3B). Collectively, these results demonstrate that the D713Y mutation does not impact hPNPase's RNA-binding or degradation activities for either single-stranded or structured RNA. However, the P467S and G499R mutations impair the enzyme's ability to both bind and degrade stem-loop RNA. Thus, these three mutations differentially affect hPNPase's activity in terms of RNA binding and degradation.

P467S and G499R mutations in hPNPase reduce S1 domain flexibility

We were intrigued that the P467S and G499R mutations, which are located on the surface of the RNase PH2 domain, could reduce the stem-loop RNA binding and degradation activities of hPNPase. In our cryo-EM structure of hPNPase in the open conformation, these two residues are positioned close to the S1 domain, in proximity to the T692 residue (Fig. 2A). Given the high flexibility of the S1 domain, mutations of P467S and G499R, which convert a non-polar side chain to a polar/basic side chain, may disturb domain–domain interactions within hPNPase. To assess if these mutations impact the flexibility of the S1 domain in hPNPase, we performed SAXS analyses on wild-type hPNPase and four mutants, i.e. PNPase-S484A, PNPase-P467S, PNPase-G499R, and PNPase-D713Y. The PNPase-S484A mutant served as a control as previous studies have demonstrated that the S484A mutant folds as a trimer, and binds ssRNA and stem-loop RNA with affinities comparable to those of wild-type hPNPase [29]. The distance distribution profiles [Patterson function, $P(r)$] for the four mutants were similar to that of wild-type hPNPase, with Dmax values ranging from 159 to 165 Å and R_g values between 40 and 44 Å (Fig. 4A). These results indicate that all forms of hPNPase maintain a stable and compact trimeric assembly. Furthermore, we generated R_g-based dimensionless Kratky

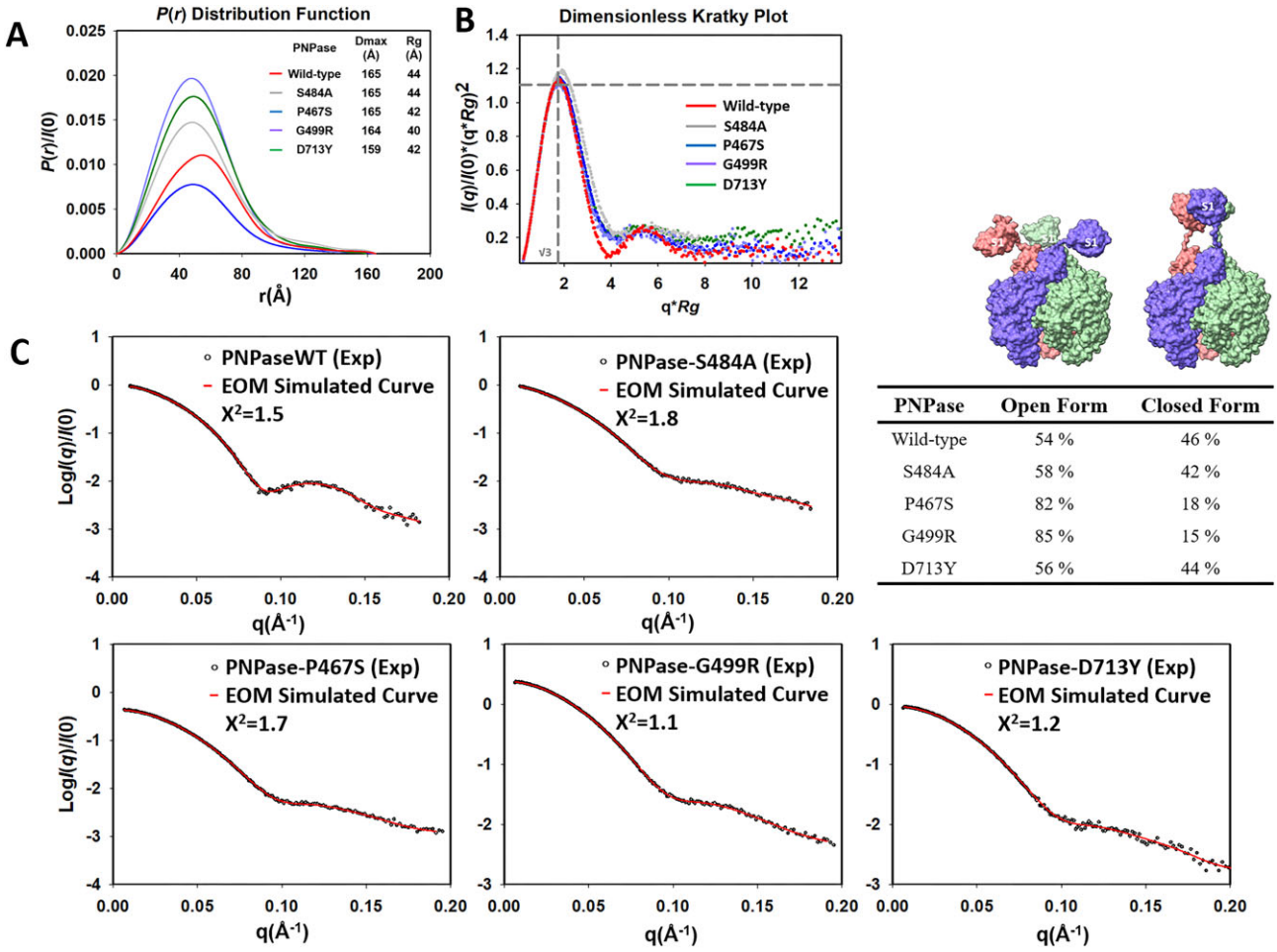

PNPase	Open Form	Closed Form
Wild-type	54 %	46 %
S484A	58 %	42 %
P467S	82 %	18 %
G499R	85 %	15 %
D713Y	56 %	44 %

Figure 4. Solution SAXS structures of hPNPase reveal a flexible S1 domain in the open and closed conformations. (**A**) The $P(r)/I(0)$ curves for wild-type and mutant hPNPase proteins are similar. (**B**) The R_g-based dimensionless Kratky plot with curve peaks at $q \times R_g > \sqrt{3}$, indicating flexible conformations. (**C**) The SAXS profiles were analyzed by the EOM. The EOM simulated curves that were calculated from a group of conformers have been fitted with the SAXS data with low χ^2 values. Wild-type and mutant hPNPase exhibit two major ensemble conformations, open and closed. Percentages of open and closed forms generated from EOM are shown in the table.

plots to assess structural flexibility. Notably, the curve peaks at $q \times R_g$ were slightly $>\sqrt{3}$, indicating that both wild-type hPNPase and the mutant variants displayed a low degree of flexibility (Fig. 4B) [52].

To explore the structural dynamics of hPNPase, we employed the EOM, which facilitates investigation of multiple conformations within a flexible protein [48]. For this approach, we utilized the crystal structure of hPNPase alongside a modeled S1 domain, treating these two components as rigid bodies during the optimization process. The experimental SAXS data correlated well with the calculated SAXS profiles from the selected ensembles of hPNPase, yielding low χ^2 values ranging from 1.1 to 1.8 (Fig. 4C). The EOM produced a collection of structures showing that the S1 domains of hPNPase exhibited flexibility, capable of adopting either a fully extended open conformation or associating with the remaining body of the enzyme in a closed conformation (Fig. 4C). For wild-type hPNPase, PNPase-S484A and PNPase-D713Y, 54%–58% of their ensembles were in the open conformation, with the remaining 42%–46% being in the closed conformation (Fig. 4C). Notably, these proportions closely resemble those observed in our cryo-EM images, which showed 52.9% (911 400) particles in the open conformation and 47.1% (811 762) particles in the closed conformation.

In contrast, the hPNPase mutants PNPase-P467S and PNPase-G499R exhibited a significant shift in their conformational dynamics. These mutants displayed two predominant conformations, with 82%–85% of their ensembles in the open conformation and only 15%–18% in the closed conformation (Fig. 4C). This outcome indicates that the P467S and G499R mutations reduce S1 domain flexibility. This decreased flexibility may impair the ability of the respective hPNPase mutants to effectively bind to the stem-loop motifs of structured RNAs, which are essential for RNA import into mitochondria and for the degradation of structured RNAs. To validate the changes in physical properties of the two variants, we measured the CD spectra and the thermal melting points of wild-type and mutated hPNPase. The CD profiles of the four mutants closely resemble that of the wild-type hPNPase, indicating that the mutations did not induce major structural perturbations or significant changes in secondary structures (Supplementary Fig. S7A). The melting points of S484A (59.1°C) and D713Y (60.1°C) are close to that of wild-type hPNPase (60.1°C) (Supplementary Fig. S7B). In contrast, the melting points of P4678S (56.0°C) and G499R (55.0°C) are significantly lower than that of the wild-type hPNPase (60.1°C), indicating a notable alteration in physical property. Together with our biochemical and biophysical data, we con-

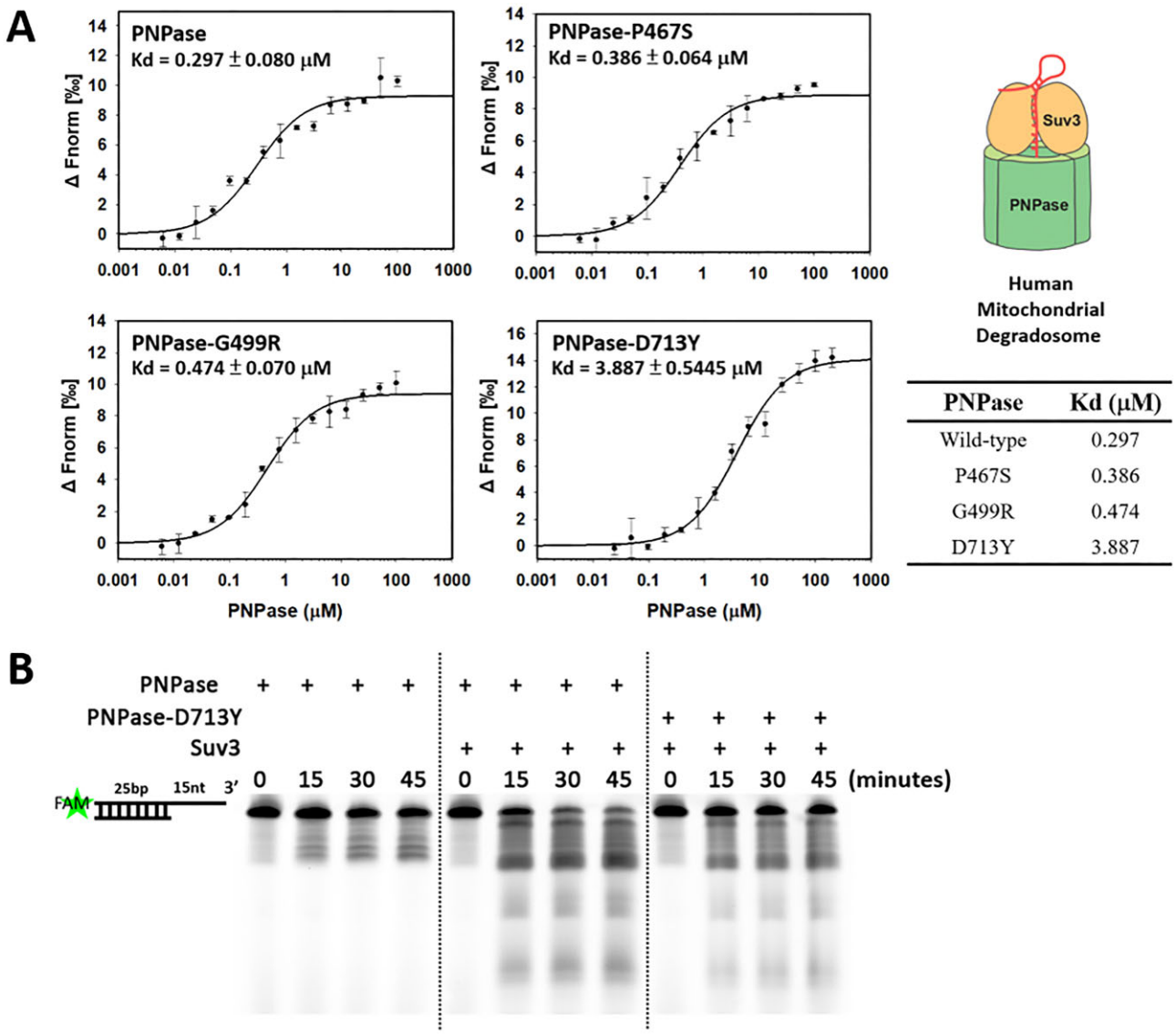

PNPase	Kd (μM)
Wild-type	0.297
P467S	0.386
G499R	0.474
D713Y	3.887

Figure 5. The D713Y mutation in hPNPase weakens the interaction between hPNPase and Suv3 helicase. (**A**) The binding affinities between Suv3 helicase and wild-type or mutant hPNPase were measured by MST. Alexa 647-labeled Suv3 (3.5 nM) was added to a 16-step serial dilution of wild-type or mutant hPNPase (P467S, G499R, and D713Y), respectively. The resulting dose–response curves plotted as mean ± SD from three independent experiments were fitted to a one-site binding model to extract K_d values using MO.Affinity Analysis software (v2.3). (**B**) In the presence of Suv3 helicase, cooperative dsRNA degradation by hPNPase and Suv3 was impaired by the D713Y mutation in hPNPase.

clude that the P467S and G499R mutations reduce hPNPase's binding and degradation activities toward structured RNA due to an impaired ability of the S1 domain to transition between the open and closed conformations, with the latter being critical for the capture of structured RNA. The resulting defects in RNA binding could ultimately disrupt cellular processes that rely on mtRNA metabolism, including RNA import and degradation.

D713Y mutation of hPNPase weakens its interactions with Suv3

The D713Y mutation in hPNPase does not affect its trimeric assembly, RNA-binding affinity, RNA degradation activity, or S1 domain flexibility, so its impacts on hPNPase functionality remained unclear. In the mitochondrial matrix, hPNPase associates with Suv3 helicase to form the mtRNA degradosome, which is essential for degrading structured RNAs [53]. This interaction between hPNPase and Suv3 is critical for maintaining efficient RNA degradation, enabling the rapid processing of RNA molecules that require regulation and turnover. To investigate whether disease-linked mutations affect assembly of the mtRNA degradosome, we measured the interaction between Suv3 and wild-type hPNPase, as well as the three hPNPase mutant variants. We prepared Alexa 647-labeled Suv3 and titrated it with varying concentrations of hPNPase. The binding affinity between Suv3 and hPNPase was then determined by MST. The normalized MST data were fitted to a logistic binding curve, yielding a dissociation constant (K_d) of 0.297 ± 0.080 μM between Suv3 and wild-type hPNPase (Fig. 5). The disease-linked P467S and G499R mutants exhibited slightly weaker affinities for Suv3 compared to wild-type hPNPase, with K_d values of 0.386 ± 0.064 and 0.474 ± 0.07 μM, respectively. These results indicate that these two mutations do not significantly impair the interaction between hPNPase and Suv3 (Fig. 5). In contrast, the PNPase-D713Y mu-

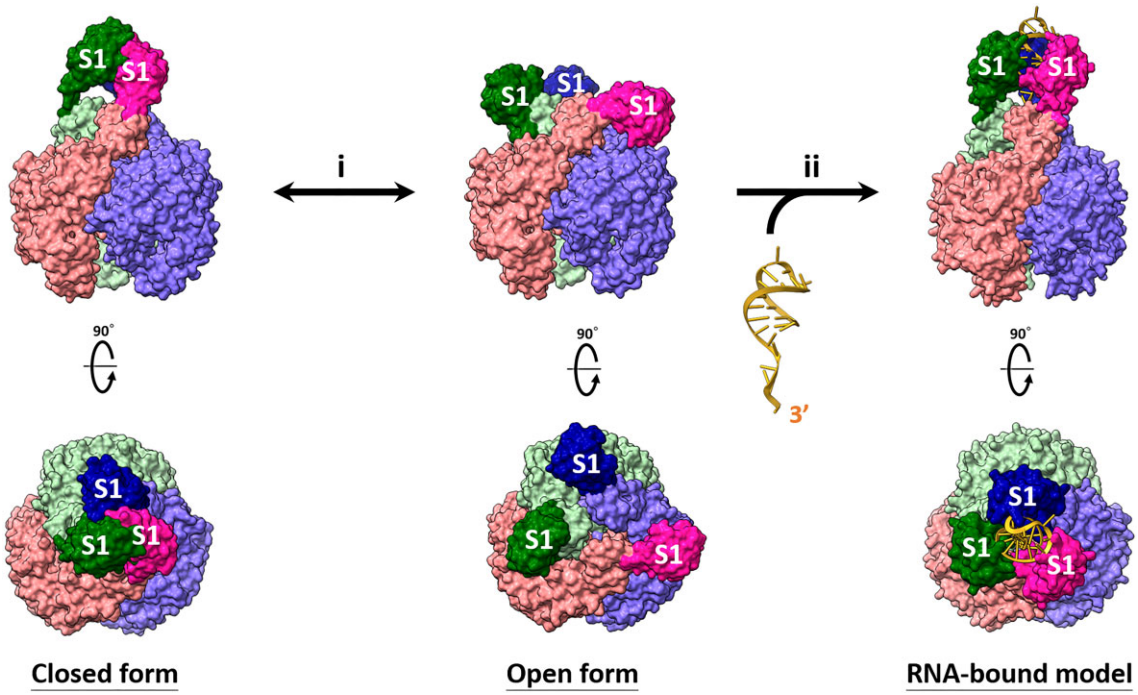

Figure 6. Proposed model of hPNPase oscillating between closed and open forms to capture and bind structured RNA. The triad of S1 domains in hPNPase is flexible, primarily adopting one of two major conformations. When it encounters structured RNA, hPNPase switches from an open to closed state, allowing its S1 domain to interact with the structured RNA. See also Supplementary Movie S1.

tant displayed a markedly different binding profile, with a 13-fold increase in K_d of 3.887 ± 0.545 μM relative to wild-type hPNPase (Fig. 5). This outcome indicates that the interaction between hPNPase and Suv3 heavily involves the S1 domain and that the D713Y mutation within this domain impairs the interaction between these two enzymes.

The significantly reduced affinity of the hPNPase-D713Y mutant underscores its detrimental impact on the interaction between hPNPase and Suv3, potentially compromising the stability of the functional RNA degradosome and affecting the efficiency of RNA degradation in the mitochondrial matrix. To validate this hypothesis, we further examined degradation of structured RNA by the combined action of hPNPase and Suv3. We incubated 5′-end FAM-labeled 25-bp dsRNA with a 15-nt 3′ overhang in a degradation buffer containing PNPase and Suv3. In the time-course experiment, hPNPase alone degraded only the 3′-ovehang RNA up to the double-stranded region. However, the addition of Suv3 significantly enhanced the degradation, enabling the efficient breakdown of dsRNA by the PNPase–Suv3 complex (Fig. 5B). In contrast, the PNPase-D713Y mutant exhibited a significantly reduced ability to degrade dsRNA in the presence of Suv3 (Fig. 5B). These findings show that D713Y mutation of hPNPase weakens its interactions with Suv3, resulting in less efficient dsRNA degradation through the cooperative mechanisms of RNA unwinding by Suv3 and RNA degradation by hPNPase.

Discussion

In this study, we present cryo-EM structures of hPNPase at near-atomic resolutions of 3.7–3.8 Å, revealing a flexible S1 domain that adopts both open and closed conformations, positioned atop the RNA-degrading chamber. By combining cryo-EM structures with SAXS and biochemical analyses, we demonstrate that the P467S and G499R mutations reduce the flexibility of the S1 domain, impeding its ability to transition between open and closed states, which is essential for binding structured RNA. The mutated residues, S467 and R499, with their longer polar/charged side chains compared to P467 and G499, may interact with nearby residues, such as T692, in the S1 domain, restricting the domain's ability to shift from the open to closed conformation. In contrast, the D713Y mutation does not affect the enzyme's RNA-binding and RNA-degrading activities, nor does it alter the flexibility of the S1 domain, yet it does weaken the interaction between hPNPase and Suv3 helicase. This disruption impairs the cooperative degradation of structured RNA by hPNPase and Suv3. Overall, our findings emphasize the critical role of S1 domain dynamics in hPNPase's ability to capture structured RNA and they underscore its involvement in protein–protein interactions with Suv3 helicase (Fig. 6 and Supplementary Movie S1).

Mammalian PNPase plays a crucial role in maintaining mitochondrial homeostasis across all cell types. As a result, knockdown or knockout of PNPase impairs mitochondrial respiration, alters mitochondrial morphology [13, 19], disrupts MRP [19], and suppresses mitochondrial mRNA decay [54]. Beyond these RNA processing defects, PNPase knockdown in mouse embryonic fibroblasts was also shown previously to promote loss of mtDNA and changes in the expression of metabolic genes, indicating a role in mtDNA maintenance [55]. Given its essential functions, it is not surprising that various biallelic pathogenic hPNPase variants have been identified, which are associated with a wide range of heterogeneous clinical phenotypes [31]. Patients carrying biallelic mutations, such as S70P/D713Y and G499R/A507S, exhibit reduced hPNPase protein levels and mitochondrial dsRNA accumulations that can leak into the cytoplasm, triggering a type I interferon response [17]. A homozygous P467S mutation

in hPNPase has been identified in a patient with AGS syndrome, characterized by abnormal type I interferon activation, early-onset encephalopathy, severe neurodevelopment regression, progressive secondary microcephaly, epilepsy, movement disorders, and white matter hyperintensities [38]. In our study, these three hPNPase mutants, i.e. P467S, G499R, and D713Y, all exhibited defects in either dsRNA binding (P467S, G499R), dsRNA degradation (P467S, G499R), or Suv3-mediated dsRNA degradation (D713Y). These defects in dsRNA degradation align with the clinical phenotypes observed in patients, including the accumulation of mitochondrial dsRNA and subsequent activation of a type I interferon response, characteristic of a disease class known as type I interferonopathies [56]. In conclusion, our findings shed light on the primary pathological mechanisms by which the P467S, G499R, and D713Y mutations of hPNPase impair dsRNA degradation. Thus, not only have we elucidated the cryo-EM structures of hPNPase and its fundamental mechanisms of RNA binding and degradation, but we also highlight the molecular defects that are induced by disease-associated mutations.

Accession number

Open form hPNPase: PDB code: 9KJR, EMDB code: EMD-62372. Closed form hPNPase: PDB code: 9KJT, EMDB code: EMD-62375.

Acknowledgements

The cryo-EM experiments were performed at the Academia Sinica Cryo-EM Facility (ASCEM). ASCEM is jointly supported by Academia Sinica Core Facility and Innovative Instrument Project (Grant No. AS-CFII-111-210) and Taiwan Protein Project (Grant No. AS-KPQ-109-TPP2). We acknowledge the staff members of the SAXS beamline TLS23A1 at the National Synchrotron Radiation Research Center, Hsin-Chu, Taiwan for assistance in the small-angle X-ray scattering experiments. We also acknowledge the Biophysics Core of the Institute of Molecular Biology for the fluorescence-based assays, as well as the Academia Sinica Biophysics Core Facility (AS-CFII-111-201) for use of the MicroScale Thermophoresis (MST) system and the Academia Sinica Sequence Core Facility (AS-CFII-113-A12).

Author contributions: Conceptualization: Y.C.L. and H.S.Y. Methodology: Y.C.L., C.H.W., M.Y., Y.P.C., and W.Z.Y. Investigation: Y.C.L. and Y.P.C. Formal analysis: Y.C.L. and C.H.W. Visualization: Y.C.L. and W.Z.Y. Writing: Y.C.L. and H.S.Y. Supervision: H.S.Y. Funding acquisition: H.S.Y.

Supplementary data

Supplementary data is available at NAR online.

Conflict of interest

None declared.

Funding

This work was supported by Academia Sinica, Taiwan, ROC (AS-IA-110-L02 to H.S.Y.). Funding to pay the Open Access publication charges for this article was provided by Academia Sinica.

Data availability

Molecular structures have been deposited in the PDB (https://www.rcsb.org/) and EMDB databases (https://www.ebi.ac.uk/emdb/): Open form hPNPase: PDB code: 9KJR, EMDB code: EMD-62372. Closed form hPNPase: PDB code: 9KJT, EMDB code: EMD-62375.

References

1. Falchi FA, Pizzoccheri R, Briani F. Activity and function in human cells of the evolutionary conserved exonuclease polynucleotide phosphorylase. *Int J Mol Sci* 2022;**23**:1652. https://doi.org/10.3390/ijms23031652
2. Cameron TA, Matz LM, Lay NRD. Polynucleotide phosphorylase: not merely an RNase but a pivotal post-transcriptional regulator. *PLoS Genet* 2018;**14**:e1007654. https://doi.org/10.1371/journal.pgen.1007654
3. Sarkar D, Fisher PB. Polynucleotide phosphorylase: an evolutionary conserved gene with an expanding repertoire of functions. *Pharmacol Ther* 2006;**112**:243–63. https://doi.org/10.1016/j.pharmthera.2006.04.003
4. Cheng ZF, Deutscher MP. Quality control of ribosomal RNA mediated by polynucleotide phosphorylase and RNase R. *Proc Natl Acad Sci USA* 2003;**100**:6388–93. https://doi.org/10.1073/pnas.1231041100
5. Cartalas J, Coudray L, Gobert A. How RNases shape mitochondrial transcriptomes. *Int J Mol Sci* 2022;**23**:6141. https://doi.org/10.3390/ijms23116141
6. Tejada-Arranz A, cy-Lagard VrdC, Reuse Hd. Bacterial RNA degradosomes: molecular machines under tight control. *Trends Biochem Sci* 2020;**45**:42–57. https://doi.org/10.1016/j.tibs.2019.10.002
7. Lehnik-Habrink M, Pfortner H, Rempeters L *et al.* The RNA degradosome in *Bacillus subtilis*: identification of CshA as the major RNA helicase in the multiprotein complex. *Mol Microbiol* 2010;**77**:958–71. https://doi.org/10.1111/j.1365-2958.2010.07264.x
8. Li Z, Deutscher MP. The role of individual exoribonucleases in processing at the 3' end of *Escherichia coli* tRNA precursors. *J Biol Chem* 1994;**269**:6064–71. https://doi.org/10.1016/S0021-9258(17)37570-1
9. Smith BA, Gupta N, Denny K *et al.* Characterization of 16S rRNA processing with pre-30S subunit assembly intermediates from *E. coli*. *J Mol Biol* 2018;**430**:1745–59. https://doi.org/10.1016/j.jmb.2018.04.009
10. Bandyra KJ, Sinha D, Syrjanen J *et al.* The ribonuclease polynucleotide phosphorylase can interact with small regulatory RNAs in both protective and degradative modes. *RNA* 2016;**22**:360–72. https://doi.org/10.1261/rna.052886.115
11. Cameron TA, Matz LM, Sinha D *et al.* Polynucleotide phosphorylase promotes the stability and function of hfq-binding sRNAs by degrading target mRNA-derived fragments. *Nucleic Acids Res* 2019;**47**:8821–37.
12. De Lay N, Gottesman S. Role of polynucleotide phosphorylase in sRNA function in *Escherichia coli*. *RNA* 2011;**17**:1172–89. https://doi.org/10.1261/rna.2531211
13. Chen H-W, Rainey RN, Balatoni CE *et al.* Mammalian polynucleotide phosphorylase is an intermembrane space RNase that maintains mitrochondrial homeostasis. *Mol Cell Biol* 2006;**26**:8475–87. https://doi.org/10.1128/MCB.01002-06
14. Slomovic S, Schuster G. Stable PNPase RNAi silencing: its effect on the processing and adenylation of human mitochondrial RNA. *RNA* 2008;**14**:310–23. https://doi.org/10.1261/rna.697308

15. Wang DD-H, Shu Z, Lieser SA *et al.* Human mitochondrial SUV3 and polynucleotide phosphorylase form a 330-kDa heteropentamer to cooperatively degrade double-stranded RNA with a 3'-to-5' directionality. *J Biol Chem* 2009;**284**:20812–21. https://doi.org/10.1074/jbc.M109.009605
16. Minczuk M, Piwowarski J, Papworth MA *et al.* Localisation of the human hSuv3p helicase in the mitochondrial matrix and its preferential unwinding of dsDNA. *Nucleic Acids Res* 2002;**30**:5074–86. https://doi.org/10.1093/nar/gkf647
17. Dhir A, Dhir S, Borowski LS *et al.* Mitochondrial double-stranded RNA triggers antiviral signalling in humans. *Nature* 2018;**560**:238–42. https://doi.org/10.1038/s41586-018-0363-0
18. Rainey RN, Glavin JD, Chen HW *et al.* A new function in translocation for the mitochondrial i-AAA protease Yme1: import of polynucleotide phosphorylase into the intermembrane space. *Mol Cell Biol* 2006;**26**:8488–97. https://doi.org/10.1128/MCB.01006-06
19. Wang G, Chen HW, Oktay Y *et al.* PNPASE regulates RNA import into mitochondria. *Cell* 2010;**142**:456–67. https://doi.org/10.1016/j.cell.2010.06.035
20. Shepherd DL, Hathaway QA, Pinti MV *et al.* Exploring the mitochondrial microRNA import pathway through polynucleotide phosphorylase (PNPase). *J Mol Cell Cardiol* 2017;**110**:15–25. https://doi.org/10.1016/j.yjmcc.2017.06.012
21. S M.F., J G.H., L B.F.. A duplicated fold is the structural basis for polynucleotide phosphorylase catalytic activity, processivity, and regulation. *Structure* 2000;**8**:1215–26.
22. Nurmohamed S, Vaidialingam B, Callaghan AJ *et al.* Crystal structure of *Escherichia coli* polynucleotide phosphorylase core bound to RNase E, RNA and manganese: implications for catalytic mechanism and RNA degradosome assembly. *J Mol Biol* 2009;**389**:17–33. https://doi.org/10.1016/j.jmb.2009.03.051
23. Shi Z, Yang WZ, Lin-Chao S *et al.* Crystal structure of *Escherichia coli* PNPase: central channel residues are involved in processive RNA degradation. *RNA* 2008;**14**:2361–71. https://doi.org/10.1261/rna.1244308
24. Hardwick SW, Gubbey T, Hug I *et al.* Crystal structure of *Caulobacter crescentus* polynucleotide phosphorylase reveals a mechanism of RNA substrate channelling and RNA degradosome assembly. *Open Biol* 2012;**2**:120028. https://doi.org/10.1098/rsob.120028
25. Unciuleac M-C, Ghosh S, Cruz MJdl *et al.* Structure and mechanism of *Mycobacterium smegmatis* polynucleotide phosphorylase. *RNA* 2021;**27**:959–69. https://doi.org/10.1261/rna.078822.121
26. Wang N, Sheng Y, Liu Y *et al.* Cryo-EM structures of *Mycobacterium tuberculosis* polynucleotide phosphorylase suggest a potential mechanism for its RNA substrate degradation. *Arch Biochem Biophys* 2024;**754**:109917. https://doi.org/10.1016/j.abb.2024.109917
27. Lin CL, Wang YT, Yang WZ *et al.* Crystal structure of human polynucleotide phosphorylase: insights into its domain function in RNA binding and degradation. *Nucleic Acids Res* 2012;**40**:4146–57. https://doi.org/10.1093/nar/gkr1281
28. Portnoy V, Palnizky G, Yehudai-Resheff S *et al.* Analysis of the human polynucleotide phosphorylase (PNPase) reveals differences in RNA binding and response to phosphate compared to its bacterial and chloroplast counterparts. *RNA* 2008;**14**:297–309. https://doi.org/10.1261/rna.698108
29. Golzarroshan B, Lin C-L, Li C-L *et al.* Crystal structure of dimeric human PNPase reveals why disease-linked mutants suffer from low RNA import and degradation activities. *Nucleic Acids Res* 2018;**46**:8630–40. https://doi.org/10.1093/nar/gky642
30. Dendooven T, Sinha D, Roeselová A *et al.* A cooperative PNPase-hfq-RNA carrier complex facilitates bacterial riboregulation. *Mol Cell* 2021;**81**:2901–13. https://doi.org/10.1016/j.molcel.2021.05.032
31. Rius R, Bergen NJV, Compton AG *et al.* Clinical spectrum and functional consequences associated with bi-allelic pathogenic PNPT1 variants. *J Clin Med* 2019;**8**:2020. https://doi.org/10.3390/jcm8112020
32. Ameln Sv, Wang G, Boulouiz R *et al.* A mutation in *PNPT1*, encoding mitochondrial-RNA-import protein PNPase, causes hereditary hearing loss. *Am J Hum Genet* 2012;**91**:919–27.
33. Vedrenne V, Gowher A, De Lonlay P *et al.* Mutation in PNPT1, which encodes a polyribonucleotide nucleotidyltransferase, impairs RNA import into mitochondria and causes respiratory-chain deficiency. *Am J Hum Genet* 2012;**91**:912–8. https://doi.org/10.1016/j.ajhg.2012.09.001
34. Matilainen S, Carroll CJ, Richter U *et al.* Defective mitochondrial RNA processing due to PNPT1 variants causes Leigh syndrome. *Hum Mol Genet* 2017;**26**:3352–61. https://doi.org/10.1093/hmg/ddx221
35. Alodaib A, Sobreira N, Gold WA *et al.* Whole-exome sequencing identifies novel variants in PNPT1 causing oxidative phosphorylation defects and severe multisystem disease. *Eur J Hum Genet* 2017;**25**:79–84. https://doi.org/10.1038/ejhg.2016.128
36. Sato R, Arai-Ichinoi N, Kikuchi A *et al.* Novel biallelic mutations in the PNPT1 gene encoding a mitochondrial-RNA-import protein PNPase cause delayed myelination. *Clin Genet* 2017;**93**:242–7. https://doi.org/10.1111/cge.13068
37. Eaton A, Bernier FP, Goedhart C *et al.* Is PNPT1-related hearing loss ever non-syndromic? Whole exome sequencing of adult siblings expands the natural history of PNPT1-related disorders. *Am J Med Genet A* 2018;**176**:2487–93. https://doi.org/10.1002/ajmg.a.40516
38. Bamborschke D, Kreutzer M, Koy A *et al.* PNPT1 mutations may cause Aicardi–Goutières syndrome. *Brain Dev* 2021;**43**:320–4.
39. Zheng SQ, Palovcak E, Armache JP *et al.* MotionCor2: anisotropic correction of beam-induced motion for improved cryo-electron microscopy. *Nat Methods* 2017;**14**:331–2. https://doi.org/10.1038/nmeth.4193
40. Punjani A, Rubinstein JL, Fleet DJ *et al.* cryoSPARC: algorithms for rapid unsupervised cryo-EM structure determination. *Nat Methods* 2017;**14**:290–6. https://doi.org/10.1038/nmeth.4169
41. Pettersen EF, Goddard TD, Huang CC *et al.* UCSF ChimeraX: structure visualization for researchers, educators, and developers. *Protein Sci* 2021;**30**:70–82. https://doi.org/10.1002/pro.3943
42. Jumper J, Evans R, Pritzel A *et al.* Highly accurate protein structure prediction with AlphaFold. *Nature* 2021;**596**:583–9. https://doi.org/10.1038/s41586-021-03819-2
43. Kidmose RT, Juhl J, Nissen P *et al.* Namdinator—automatic molecular dynamics flexible fitting of structural models into cryo-EM and crystallography experimental maps. *IUCrJ* 2019;**6**:526–31. https://doi.org/10.1107/S2052252519007619
44. Adams PD, Afonine PV, Bunkoczi G *et al.* PHENIX: a comprehensive Python-based system for macromolecular structure solution. *Acta Crystallogr D Biol Crystallogr* 2010;**66**:213–21. https://doi.org/10.1107/S0907444909052925
45. Emsley P, Cowtan K. Coot: model-building tools for molecular graphics. *Acta Crystallogr D Biol Crystallogr* 2004;**60**:2126–32. https://doi.org/10.1107/S0907444904019158
46. Konarev PV, Volkov VV, Sokolova AV *et al.* PRIMUS: a Windows PC-based system for small-angle scattering data analysis. *J Appl Crystallogr* 2003;**36**:1277–82. https://doi.org/10.1107/S0021889803012779
47. Svergun D. Determination of the regularization parameter in indirect-transform methods using perceptual criteria. *J Appl Crystallogr* 1992;**25**:495–503. https://doi.org/10.1107/S0021889892001663
48. Petoukhov MV, Franke D, Shkumatov AV *et al.* New developments in the ATSAS program package for small-angle scattering data analysis. *J Appl Crystallogr* 2012;**45**:342–50. https://doi.org/10.1107/S0021889812007662
49. Franklin MC, Cheung J, Rudolph MJ *et al.* Structural genomics for drug design against the pathogen *Coxiella burnetii*. *Proteins* 2015;**83**:2124–36. https://doi.org/10.1002/prot.24841

50. Miles AJ, Ramalli SG, Wallace BA. DichroWeb, a website for calculating protein secondary structure from circular dichroism spectroscopic data. *Protein Sci* 2022;**31**:37–46. https://doi.org/10.1002/pro.4153
51. Wong AG, McBurney KL, Thompson KJ *et al.* S1 and KH domains of polynucleotide phosphorylase determine the efficiency of RNA binding and autoregulation. *J Bacteriol* 2013;**195**:2021–31. https://doi.org/10.1128/JB.00062-13
52. Receveur-Brechot V, Durand D. How random are intrinsically disordered proteins? A small angle scattering perspective. *Curr Protein Pept Sci* 2012;**13**:55–75. https://doi.org/10.2174/138920312799277901
53. Borowski LS, Dziembowski A, Hejnowicz MS *et al.* Human mitochondrial RNA decay mediated by PNPase–hSuv3 complex takes place in distinct foci. *Nucleic Acids Res* 2013;**41**:1223–40. https://doi.org/10.1093/nar/gks1130
54. Chujo T, Ohira T, Sakaguchi Y *et al.* LRPPRC/SLIRP suppresses PNPase-mediated mRNA decay and promotes polyadenylation in human mitochondria. *Nucleic Acids Res* 2012;**40**:8033–47. https://doi.org/10.1093/nar/gks506
55. Shimada E, Ahsan FM, Nili M *et al.* PNPase knockout results in mtDNA loss and an altered metabolic gene expression program. *PLoS One* 2018;**13**:e0200925. https://doi.org/10.1371/journal.pone.0200925
56. Lee-Kirsch MA. The type I interferonopathies. *Annu Rev Med* 2017;**68**:297–315. https://doi.org/10.1146/annurev-med-050715-104506

Received: November 25, 2024. **Revised:** January 23, 2025. **Editorial Decision:** February 4, 2025. **Accepted:** February 7, 2025